Oil & Gas Science and Technology – Rev. IFP, Vol. 56 (2001), No. 2, pp. 161-179

Detection of Metal Defects on Gas Distribution Pipeline by Remote Field Eddy Current (RFEC) Using Finite-Element Analysis

J.H. Yang[1] and Y.S. Yoon[2]

1 R&D Center, Seoul City Gas Co., Ltd., 236-1 Duckee-Dong, Ilsan-Ku, Koyang City, Kyungki-Do, 411-450 - Korea
2 Department of Mechanical Engineering, Korea Advanced Institute of Science and Technology, 373-1 Kusung-Dong, Taejun - Korea
e-mail: jhyang@seoulgas.co.kr - ysyoon@kaist.ac.kr

Résumé — Analyse par la méthode des éléments finis de la détection des défauts métalliques d'un gazoduc en utilisant les courants de Foucault en champ lointain — Pour établir des stratégies sécurisées de remplacement et maintenance des gazoducs souterrains, il est nécessaire de détecter leurs défauts métalliques, classifiés de la manière suivante : corrosion générale, fissuration par corrosion sous contrainte, lamination, trou, pertes métalliques provoquant des fuites et dommages partiels. C'est la raison pour laquelle une méthode efficace doit être développée, qui permette une inspection en ligne à l'intérieur du gazoduc.

Dans cette étude, les formulations théoriques du potentiel vecteur magnétique et de la densité du flux magnétique, utilisant les nombres d'onde axial and radial basés sur les équations de Maxwell, sont présentées analytiquement pour évaluer les variations d'amplitude et de phase de la densité du flux magnétique, ainsi que la tension induite. Ces résultats peuvent constituer les critères d'application du principe d'utilisation des courants de Foucault en champ lointain pour détecter les défauts métalliques d'un gazoduc. Un calcul tridimensionnel par la méthode des éléments finis est également présenté pour analyser les défauts dans le métal en relation avec leur taille, la fréquence d'excitation et la vitesse de déplacement. Cette approche en trois dimensions permet de pallier l'inexactitude de l'approche bidimensionnelle axisymétrique, et peut simuler la présence de trous locaux dans les gazoducs. À défaut de cette approche, seules des pertes métalliques homogènes, comme par exemple la diminution de l'épaisseur de la paroi, peuvent être modélisées.

Les résultats de l'analyse par éléments finis concernant la densité de flux magnétique et la tension induite dans le détecteur sont comparés à ceux d'études expérimentales.

Mots-clés : courants de Foucault en champ lointain, densité de flux, tension induite, excitatrice, détecteur.

Abstract* — *Detection of Metal Defects on Gas Distribution Pipeline by Remote Field Eddy Current (RFEC) Using Finite-Element Analysis — *It is necessary to find out whether there are metal defects on underground gas distribution pipelines without excavation in order to establish safety strategies for replacement or maintenance. The metal defects are classified into general corrosion, stress corrosion cracking, lamination, pits, and metal loss, which cause leak or partial damages to a gas pipeline. Therefore, it is required to develop an effective method in the form of an in-line inspection concept that could be implemented internally into a gas pipeline.*

In this study, theoretical formulations of the magnetic vector potential and magnetic flux density including axial and radial wave numbers based on Maxwell equations are presented analytically to find out the changes of amplitude and phase in the magnetic flux density and the consequent induced voltage which can be a criterion in the remote field eddy current principle for detecting the metal defects in gas pipelines. Three-dimensional finite-element analysis is also presented to analyze the physical phenomenon in metal defects according to each defect size, excitation frequency and moving velocity, which can overcome inaccuracy of the two-dimensional approach, using axisymmetry condition, and simulate local pit conditions occurred severely in real gas pipelines; otherwise only metal loss such as whole circumferential decrease in wall thickness can be modeled.

Some experimental works are performed to validate the analytical and finite elemental results regarding the magnetic flux density and induced voltage in the detector.

Keywords: remote field eddy current (RFEC), flux density, induced voltage, exciter, detector.

INTRODUCTION

Pipelines are essential for fluid transmission, and as most oil or gas pipelines are buried, safety of underground pipelines becomes very important as their distribution has expanded so far. Therefore, it is important to inspect the status of pipelines accurately, in particular, city gas pipelines that have been buried for tens of years.

There may be various methodologies to detect metal defects of pipelines, such as corrosion, lamination and crack. But some of the most representing methods are ultrasonics, Magnetic Flux Leakage (MFL), and eddy current of which studies have been done actively. In particular, MFL or eddy current may be more proper for gas pipelines than ultrasonics, which requires couplant as they should be inspected in live gas status. Recently, MFL has been applied to intelligent pigs for precise inspection of large-scale transmission pipelines as a result of theoretical studies of flux leakage (Mandayam *et al.*, 1996).

In order to implement this method, it should be condensed as a physical sensor form and should be ultimately linked to a self-propelled robot which could move on its own inside the pipelines. Studies of the robot itself (Kawaguchi *et al.*, 1995) have been actively performed to implement this methodology.

The purpose of this study is to develop an analytical method and a finite-element analysis method to detect metal defects using Remote Field Eddy Current (RFEC) which is an active method similar to MFL but more suitable for inspecting the city gas distribution pipelines (small-diameter and low-pressure pipelines).

RFEC is a technique developed to overcome the skin effect (Lowther and Silvester, 1985) that has been shown in the conventional eddy current. Schmidt (1984) showed in his experiments that the signal is detected at the same sensitivity whether there is internal or external defects (corrosion) of the pipeline. Atherton *et al.* (1987) performed finite-element analysis for the cases of having corrosion and having no corrosion, using the two-dimensional axisymmetric model to explain the characteristics of RFEC, which initiated the study of axial cracks by Sun *et al.* (1992). Studies, mainly on Finite Element Method (FEM) (2D) approach, have been continued (Atherton *et al.*, 1988; Lord *et al.*, 1988; Sun, 1989).

Chen *et al.* (1992) studied changes in the magnetic flux and voltage response in the detector in accordance with time with a sinusoidal excitation frequency of 80 Hz. Atherton and Czura (1994) modeled pipeline corrosion as a slot in the finite element to transform width and depth of the slot into variables to quantify changes in the magnetic vector potential, pointing vector and magnetic field intensity *(H)*. Based on the experimental result that metal defects change the external as well as the internal fields, Atherton *et al.* (1994) reviewed changes in the external field as an indication of a minor change in the field propagation through the defects (changes in amplitude and phase), and Mergelas and Atherton (1996) recently provided various explanations on the changes in the amplitude and phase of the magnetic flux density when there is a defect. Sutherlande and Atherton (1997) undertook an experimental approach on the influence of stress (elastic, plastic, remnant) and curvature in pipelines and showed that elastic and remnant stress at certain excitation frequency results in the same influence as metal defects.

The principle of RFEC is to use an exciter and a detector that are composed of coils with the same concept inside the pipelines. The exciter produces harmonic pulse (circumferential direction) resulting in a direct field (direct energy flow) directly flowing inside the pipelines and an indirect field flowing outside the pipelines. Then, the detector located 2*D*-3*D* (*D*: diameter of the pipeline) from the exciter can detect the resultants of these two fields. The amplitude of the direct field is attenuated rapidly while the indirect field is attenuated relatively slowly (direct field zone) resulting in a slight deeping phenomenon at the transition zone (1*D*-2*D* distant from the exciter), and there is a slight declining at the remote field zone (2*D* and further) (magnetic flux and magnetic vector potential). This is the key point of RFEC that the amplitude and phase at the remote field change when there is a metal defect such as corrosion (internal or external).

In general, the eddy current generates a field in the opposite direction to the existing field as shown in Maxwell's Equation (1) when there is a change in the amplitude or direction of the source current for the material having a conductivity σ (conductor such as steel):

$$\nabla \times E = -\frac{\partial B}{\partial t} \tag{1}$$

where E is the electric field intensity and B is the magnetic flux density. RFEC can cause an interaction (changes in amplitude and phase) through complicated actions of remote and direct fields generated by excitation (alternating current—AC—, harmonic) of the source current at the exciter, as in the formula related to the eddy current, Equation (1). As a consequence, it can detect a defect.

Firstly, this study is focusing on finding a closed-form solution for the magnetic vector potential (A_r, A_θ, A_z) and magnetic flux density (B_r, B_θ, B_z) based on Maxwell's equation and analyzing the changes in the amplitude and phase of the field for harmonic excitation of the source current in case of having metal defects and in case of having no metal defects. As explained in the background of the study, this type of formulation has been done in the past. However, this study requires that independent variables for all fields should be represented with radial r and axial z directions simultaneously to obtain a proper solution as the geometric shape of the pipeline interacting with RFEC is three-dimensional. The two-dimensional planar solution (Mackintosh *et al.*, 1993) has the problem of missing the interaction effect of wave numbers shown in Equation (2):

$$k_{pz} = \sqrt{k_{pr}^2 + j\sigma\mu\omega} \tag{2}$$

where k_{pz} and k_{pr} are the wave numbers in the axial and radial directions in the pipe material respectively, σ is the conductivity (Theodoulis and Tsiboukis, 1995), μ is the permeability, and ω is the excitation frequency.

Secondly, this study examines changes in amplitude and phase thoroughly by performing three-dimensional finite-element analysis according to the depth of the defect (corrosion), based on the above formulation. As stated before, when trying to find a solution through two-dimensional axisymmetric analysis, the magnetic vector potential A_z, perpendicular to the plane, is transformed into A_θ, which is the θ-direction potential at actual three dimensions. In this case, the geometric figure of the pipeline is axisymmetric but it has an intrinsic problem, because the actual distribution of the magnetic flux density is not necessarily symmetric when there is a local defect. Therefore, this study emphasizes explanations for why three-dimensional finite-element analysis is necessary, and furthermore reasons why such boundary conditions as cyclic symmetry, *e.g.* Neumann condition (parallel flux) or Dirichlet condition (normal flux), cannot be applied, in order to save computing time. On the other hand, as exact measurement of the magnetic flux density at a specific location is not so easy, the induced voltage caused by its change should be measured. For this, some experimental works are done.

Thirdly, this study reviews the effect on speed, *i.e.*, changes in amplitude and phase, to explain the effect of the velocity-induced current on RFEC through closed-form solution and FEM, respectively as the actual exciter and detector are installed into a robot moving inside the pipelines. It shows that the effect of a moving conductor results in transition and distortion of field distribution, and also introduces a criterion of the effect on speed by presenting quantitative change of amplitude in accordance with specific speed. Its accuracy is explained through the magnetic Reynolds number (M_{RE}).

Lastly, this study reviews changes in the amplitude and phase of the induced voltage, when there is a defect (corrosion) and when there is no defect, according to variables such as excitation frequency and core material within the detector.

1 MAGNETIC FLUX DENSITY FOR DETECTING DEFECTS

1.1 Analysis of Magnetic Flux Density

As shown in Figure 1, in order to realize RFEC when transmitting harmonic pulse (AC, circumferential) from the exciter by having an exciter and a detector composed of coils with the same concept, a direct field (direct energy flow) flowing directly inside the pipeline and an indirect field flowing externally are generated.

The model is composed of the pipe, air inside the pipe and exciter coil and earth outside the pipe, in order to apply Maxwell's diffusion equation. Relative permeabilities of the pipe, internal air and external earth are μ, μ_0 ($\mu_0 = 4\pi \times 10^{-7}$ H/m) respectively. The electric conductivity of the pipe

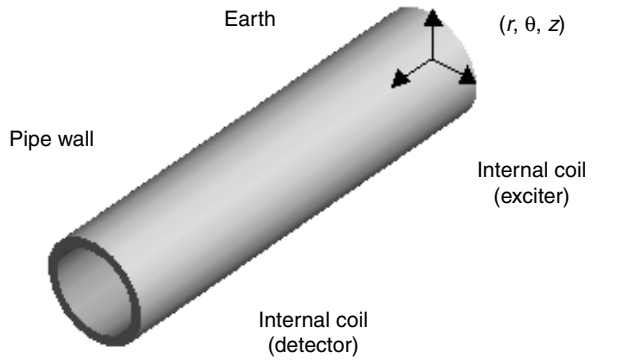

Figure 1

Model of the air-pipe-exciter-detector system.

is σ and physical properties of all materials are assumed to be isotropic. The magnetic vector potential *(A)* and the flux density *(B)* are generalized including *r*, θ, and *z* in cylindrical coordinates as in Equations (3)-(7):

$$A = e_r A_r + e_\theta A_\theta + e_z A_z \tag{3}$$

$$B = e_r B_r + e_\theta B_\theta + e_z B_z \tag{4}$$

$$B = \nabla \times A \tag{5}$$

$$\frac{1}{\mu} \nabla \times (\nabla \times B) = -\sigma \frac{\partial B}{\partial t} \tag{6}$$

$$\frac{1}{\mu} \nabla \times (\nabla \times A) = J \tag{7}$$

where J is the current density (A/m^2) representing the excitation current in the exciter coil or the eddy current induced in the pipe by electric conductivity. Using Equation (7) for the internal air and external earth, and Equation (6) for the pipe, Maxwell's equation becomes as follows (Ida and Bastos, 1997):

$$\frac{\partial}{\partial r}\left(\frac{\partial A_\theta}{\partial r}\right) + \frac{1}{r}\frac{\partial A_\theta}{\partial r} - \frac{A_\theta}{r^2} + \frac{\partial}{\partial z}\left(\frac{\partial A_z}{\partial z}\right) = J_\theta \text{ in coil} \tag{8}$$

$$\frac{\partial}{\partial r}\left(\frac{\partial A_\theta}{\partial r}\right) + \frac{1}{r}\frac{\partial A_\theta}{\partial r} - \frac{A_\theta}{r^2} + \frac{\partial}{\partial z}\left(\frac{\partial A_z}{\partial z}\right) = 0 \text{ in air} \tag{9}$$

$$\frac{\partial}{\partial r}\left(\frac{\partial B_z}{\partial r}\right) + \frac{1}{r}\frac{\partial B_z}{\partial r} + \frac{\partial}{\partial z}\left(\frac{\partial B_z}{\partial z}\right) = \sigma\mu \frac{\partial B_z}{\partial t} \text{ in pipe} \tag{10}$$

$$B = e_r\left(\frac{1}{r}\frac{\partial A_z}{\partial \theta} - \frac{\partial A_\theta}{\partial z}\right) + e_\theta\left(\frac{\partial A_r}{\partial z} - \frac{\partial A_z}{\partial r}\right) + \frac{e_z}{r}\left(\frac{\partial (rA_\theta)}{\partial r} - \frac{\partial A_r}{\partial \theta}\right) \tag{11}$$

In these equations, we can see that the dominant component of the magnetic vector potential is in the θ-direction and the consequent component of the magnetic flux density in accordance with this potential is in the *z*-direction. When we assume that there is no change of the potential and flux density in the circumferential direction, the solution of the vector potential in the internal air after applying Equation (9) (subscript θ is omitted) becomes (Gustafson, 1980):

$$A_a(r, z, t) = \left(c1\, J_1(kr) + c2\, Y_1(kr)\right) e^{-kz}\, e^{j\omega t}$$
$$k = k_{ar} = k_{az} \tag{12}$$

where J_1 and Y_1 are Bessel functions of first and second kinds, and k is the axial wave number in the air. In the air, the radial wave number is identical to the axial wave number and the last term in Equation (12) is the harmonic response to the exciter frequency. Since the potential at $r = 0$ is:

$$Y_1(0) = -\infty$$

therefore, the coefficient *c2* should be zero according to the finite boundary.

Applying the same Equation (9) to the external earth, the solution of the potential in this region becomes as follows:

$$A_e(r, z, t) = \left(c3\, H_1^1(kr) + c4\, H_1^2(kr)\right) e^{-kz}\, e^{j\omega t}$$
$$H_1^{1,2}(kr) = J_1(kr) \pm j\, Y_1(kr) \tag{13}$$

where *H* represents Hankel function (Hildebrand, 1976) and should meet the finite boundary as *r* approaches infinity:

$$r \to \infty$$

$$H_1^1(kr) \approx \sqrt{\frac{2}{\pi(kr)}}\, e^{j[kr - \pi/4 - \pi/2]} \tag{14}$$

Hence, *c3* becomes zero at infinite of the boundary if the imaginary part of k, $Im(k) < 0$. From Equations (11)-(13), the solutions of the magnetic flux density in the internal air and external earth are as follows (subscript *a* represents internal air and *e* represents external earth):

$$B_a(r, z, t) = k\left(c1\, J_0(kr) + c2\, Y_0(kr)\right) e^{-kz}\, e^{j\omega t} \tag{15}$$

$$B_e(r, z, t) = k\left(c3\, H_0^1(kr) + c4\, H_0^2(kr)\right) e^{-kz}\, e^{j\omega t} \tag{16}$$

Next, to obtain a solution for the pipe, it is convenient to use Equation (10) because the induced eddy current J is not zero as shown in Equations (8) and (9), and furthermore is unknown. Suppose $B_p(r, z, t)$ has the form of:

$$B_p(r, z, t) = R(r)Z(z)T(t)$$

Then, Equations (7) and (8) become as follows after inserting this form into Equation (9):

$$r^2 \frac{d^2R(r)}{dr^2} + r \frac{dR(r)}{dr} + (k_{pr}r)^2 R(r) = 0 \tag{17}$$

$$\frac{d^2Z(r)}{dr^2} - k_{pz}{}^2 Z(r) = 0 \tag{18}$$

$$k_{pz} = \sqrt{k_{pr}{}^2 + j\sigma\mu\omega} \tag{19}$$

In Equation (19), k_{pr} and k_{pz} mean the radial and axial wave numbers. Therefore, from Equations (17) and (18), the flux density and vector potential in the pipe are:

$$B_p(r, z, t) = \left(c7\, J_0(k_{pr}r) + c8\, Y_0(k_{pr}r)\right) e^{-k_{pz}z}\, e^{j\omega t} \tag{20}$$

$$A_p(r, z, t) = \frac{1}{k_{pr}}\left(c7\, J_0(k_{pr}r) + c8\, Y_0(k_{pr}r)\right) e^{-k_{pz}z}\, e^{j\omega t} \tag{21}$$

Boundary conditions should be satisfied at each boundary such as the inner and outer walls of the pipe. They mean the continuity of the magnetic field intensity in the tangential direction and the continuity of the magnetic vector potential at each boundary. Therefore, these boundary conditions are:

$$A_a(r1,\ z,\ t) = A_p(r1,\ z,\ t) \tag{22}$$

$$A_e(r2,\ z,\ t) = A_p(r2,\ z,\ t) \tag{23}$$

$$\frac{B_a(r1,\ z,\ t)}{\mu_0} = \frac{B_p(r1,\ z,\ t)}{\mu} \tag{24}$$

$$\frac{B_e(r2,\ z,\ t)}{\mu_0} = \frac{B_p(r2,\ z,\ t)}{\mu} \tag{25}$$

$$k = k_{pz} \tag{26}$$

Because each coefficient *c1*, *c3*, *c7*, *c8*, *k*, k_{pr} is a form of the complex number, and solutions for Bessel and Hankel functions are not closed-forms, it is not easy to solve them. From the above equations, the solution of flux density and vector potential for the pipe is obtained by solving unknown coefficients through a numerical method. For this, specific data related to the pipe are used: the relative permeability of the pipe is 70, its outside diameter is 50 mm, the thickness of the pipe wall is 6 mm, the electric conductivity is 7×10^6 (1/Ωm), and the excitation frequency is 10 Hz.

The next step consists in formulating the vector potential and the flux density when there is a metal defect, which is assumed to have width of 2 mm and depth of 50% of the wall thickness at a distance of 80 mm (z^0) from the origin. Then, exact solutions for the pipe are Equations (20) and (21) up to z^0. The solutions are as follows for the defect region from z^0:

$$\begin{aligned} B_p'(r, z, t) &= B_p(r, z, t) \qquad 0 < z < z^0 \\ &= \left(c9\, J_0(k_{pr}r) + c10\, Y_0(k_{pr}r)\right) e^{-k_{pz}z}\, e^{j\omega t} \qquad z > z^0 \end{aligned} \tag{27}$$

$$\begin{aligned} A_p'(r, z, t) &= A_p(r, z, t) \qquad 0 < z < z^0 \\ &= \frac{1}{k_{pr}}\left(c11\, J_0(k_{pr}r) + c12\, Y_0(k_{pr}r)\right) e^{-k_{pz}z}\, e^{j\omega t} \qquad z > z^0 \end{aligned} \tag{28}$$

Also, continuity should be satisfied at the defect region:

$$B_p'(r^0, z^0, t) = B_p(r^0, z^0, t) \tag{29}$$

$$A_p'(r^0, z^0, t) = A_p(r^0, z^0, t) \tag{30}$$

where r^0 represents the axial distance from the origin to the defect. From Equations (27)-(30), solutions are obtained in the same way as previously when there was no defect. Figure 2 shows that the amplitude attenuation of the magnetic flux density in the inner wall of the pipe in the remote field region decreases when there is a defect.

In other words, the amplitude increases more than in case of no defect. Figure 3 shows that the phase lag of the flux density in the inner wall of the pipe near the defect region increases. This result is coincident with that of past experiments and finite-element analysis by others as mentioned in the Introduction. In this study, wave propagation can be shown in accordance with both axial and radial wave numbers.

From now on, three-dimensional finite-element analysis is presented to show the interaction phenomenon related to the defect and to show quantitative analysis in detail when there is a defect. The finite-element model is composed of the internal air, pipe, external earth, exciter and detector coils as shown in Figure 1. The geometry of this model seems to be axisymmetric, but it is improper to use a two-dimensional approach because there is a circumferential dependence, which is verified from the above results by the fact of wave propagation according to axial and radial wave numbers.

It is important to consider that a pit is only a local defect, not a whole circumferential defect. This kind of defects is

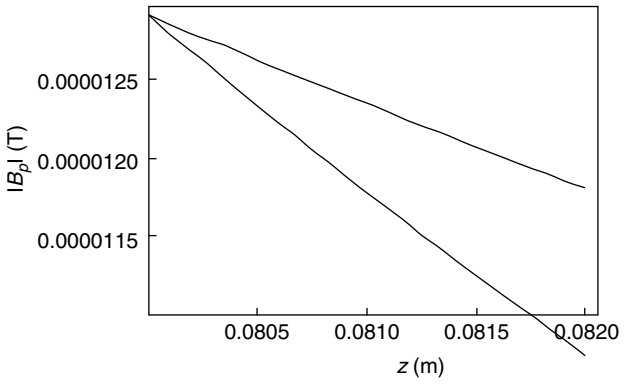

Figure 2

Change in the amplitude B_p at the defect region (upper: defect of 2 × 3 mm; lower: no defect).

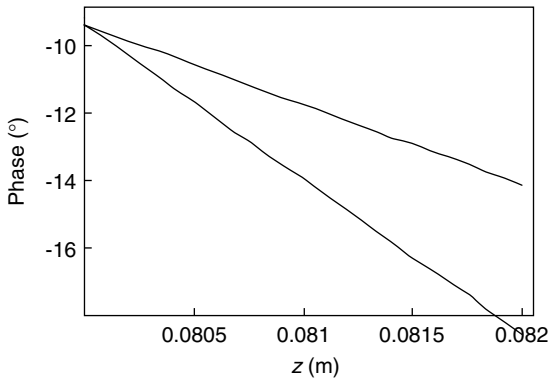

Figure 3

Change in the phase B_p at the defect region (upper: no defect; lower: defect of 2 × 3 mm).

very dangerous to gas distribution pipelines. Only three-dimensional analysis can deal with them. That is the reason why three-dimensional finite-element analysis is used.

To reduce computing time, it is generalized to use specific boundary conditions. Regarding boundary conditions for finite-element analysis, Neumann and Dirichlet conditions are excluded because there is no evidence for parallel or normal flux, even cyclic symmetry. This is due to a local defect (pit) which has a property of circumferential dependence. A singular point in central axis in internal air is avoided by using a full model instead of a half-model, and an infinite boundary element is used for the far external surface in which the magnetic vector potential should be zero. This concept is also applied to far axial distance by including an 8*D* length, in which the RFEC region is about 2*D*. The physical properties are the same as in the analytical approach. Total 42 680 elements and 45 103 nodes are used for the full model with four degrees of freedom (A_r, A_θ, A_z, voltage) assigned to each node in the pipe model while three are assigned to others.

From the finite-element results, Figures 4 and 5 show the amplitude and phase distributions of the magnetic flux density at the inner wall of the pipe along the axial distance, especially at the defect region. Each data corresponds to a specific defect of varying depth, from 12.5% to 87.5% of the wall thickness. The defect is assumed to be a rectangular shape with fixed width of 2 mm and length of 2 mm. These graphs show that the attenuation of the amplitude decreases and the phase lag increases when there is a defect in the remote field region, and that the depth of a defect can be estimated *via* the ratio of the less attenuated amplitude to the normal one (or the ratio of the increased phase lag to the normal lag). These are the characteristics of RFEC. Therefore, this study shows that certain relations or transfer functions can be derived when there is a defect.

1.2 Effect of Detector Velocity on Flux Density

In general, the velocity-induced current is generated when a conductor moves in the flux field and often this phenomenon occurs largely due to the high rotation velocity in case of induction motor, resulting in decrease of the torque (Brown and Jaroudi, 1992). In this study of detecting a metal defect, since each exciter coil and detector coil installed on a type of in-pipe robot moves inside the pipe, there are complicated relations between the common eddy current and the velocity-induced eddy current. Some studies about this velocity effect on the eddy current deal with the coordinate transformation and moving conductor (Muramatsu *et al.*, 1992; Allen *et al.*, 1995; Liu *et al.*, 1995; Song and Ida, 1992). The velocity effect of the moving detector is explained when detecting a metal defect by generalizing Maxwell's equations with inclusion of the velocity-induced current. If we assume that the exciter and detector move with a velocity of v (m/s) in the negative direction of the z-axis, then the effect of the moving conductor occurs in the pipe due to its relatively large conductivity. In other words, we can think that the pipe moves along the $+z$-axis with velocity v to the field generated by the exciter. Adding the velocity-induced current to Equation (6), then Equation (6) becomes:

$$\frac{1}{\mu}\nabla\times(\nabla\times B) = -\sigma\left(\frac{\partial B}{\partial t} - \nabla\times(v\times B)\right) \qquad (31)$$

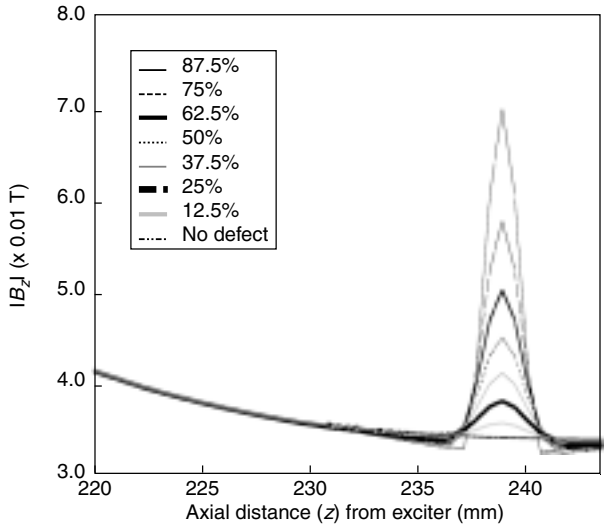

Figure 4

Amplitude of the flux density B_z (upper: defect of 87.5%; lower: defect of 12.5%).

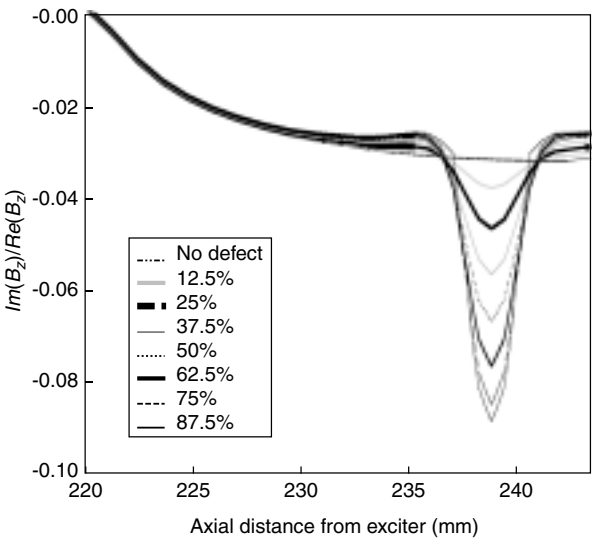

Figure 5

Phase of the flux density B_z (upper: defect of 87.5%; lower: defect of 12.5%).

Since:

$$\nabla \times (\nabla \times B) = \nabla (\nabla \cdot B) - \nabla^2 B$$

then, inserting this into Equation (31):

$$\nabla^2 B = \sigma\mu \left(\frac{\partial B}{\partial t} - \nabla \times (v \times B) \right) \tag{32}$$

Equation (32) means diffusion equation in which both first term of right-hand side that is a change of flux according to time and second term that is a change of flux due to movement make a resultant loss term as in the left-hand side.

In Equation (32), we can exclude the first term time-variant flux change in the right-hand side when we are in the viewpoint of moving coordinate, if we wish to obtain flux density varying only according to time. Alternatively, we can think of only a time-variant term replacing the velocity term in the viewpoint of stationary coordinate. In this case, the geometric shape and properties have velocity-dependent characteristics. Verification or physical compatibility for this fact is described by the magnetic Reynolds number (M_{RE}) (Woodson, 1968) as in Equation (33). If we neglect the time-variant term, this number can be a criterion for this because M_{RE} itself explains the ratio of loss to flux change by movement:

$$M_{RE} = \sigma\mu l v \tag{33}$$

However, it is important that we cannot consider only one viewpoint regarding the moving coordinate or the stationary coordinate because the velocity of the moving conductor interacts with the harmonic excitation of the exciter. Therefore:

$$\nabla \times (v \times B) = e_r \left(- v \frac{\partial B_r}{\partial z} \right) + e_\theta \left(- v \frac{\partial B_\theta}{\partial z} \right) + e_z \frac{1}{r} \frac{\partial}{\partial r} (r v B_r) \tag{34}$$

Equation (32) can be decomposed by r and z components using Equation (34):

– z component:

$$\frac{\partial^2 B_z}{\partial r^2} + \frac{1}{r} \frac{\partial B_z}{\partial r} + \frac{\partial^2 B_z}{\partial z^2} - \sigma\mu v \frac{1}{r} \frac{\partial}{\partial r} (r B_r) = \sigma\mu \frac{\partial B_z}{\partial t} \tag{35}$$

– r component:

$$\frac{\partial^2 B_r}{\partial r^2} + \frac{1}{r} \frac{\partial B_r}{\partial r} + \frac{\partial^2 B_r}{\partial z^2} - \sigma\mu v \frac{\partial B_r}{\partial z} = \sigma\mu \frac{\partial B_r}{\partial t} \tag{36}$$

Since Equation (35) is coupled, it is convenient to use the following divergence theorem (continuity) for flux:

$$\nabla \cdot B = 0 \tag{37}$$

$$\frac{1}{r} \frac{\partial}{\partial r} (r B_r) + \frac{\partial B_z}{\partial z} = 0 \tag{38}$$

Hence, from Equations (35) and (38), pure B_z becomes as follows:

$$\frac{\partial^2 B_z}{\partial r^2} + \frac{1}{r} \frac{\partial B_z}{\partial r} + \frac{\partial^2 B_z}{\partial z^2} - \sigma\mu v \frac{\partial B_z}{\partial z} = \sigma\mu \frac{\partial B_z}{\partial t} \tag{39}$$

Let:

$$B_z(r, z, t) = R(r)Z(z)T(t) \tag{40}$$

$$T(t) = e^{j\omega t} \tag{41}$$

Then, from Equations (39)-(41):

$$B_z(r, z, t) = \left(a1\, J_0(\xi r) + a2\, Y_0(\xi r) \right) e^{-\gamma z} e^{j\omega t} \tag{42}$$

where J_0 and Y_0 are Bessel functions of first and second kinds and can be represented by the following equations (ξ and γ: mean radial and axial wave numbers when there is a defect, and $a1$ and $a2$: mean coefficients):

$$J_0(\xi r) = \sum_{n=0}^{\infty} \frac{(-1)^n (\xi r/2)^{2n}}{(n!)^2}$$

$$Y_0(\xi r) = \frac{2}{\pi} \left[\left\{ \log(\xi r/2) + \chi \right\} J_0(\xi r) + \sum_{n=0}^{\infty} (-1)^{n+1} \varphi(n) \frac{(\xi r/2)^{2n}}{(n!)^2} \right]$$

with: χ : Euler' s constant, $\varphi(n) = \sum_{m=1}^{n} \frac{1}{m}$

$$\gamma L = j \left(\frac{M_{RE}}{2} \right) \pm j \sqrt{\left(\frac{M_{RE}}{2} \right)^2 + \left[(\xi L)^2 + j\, 2 \left(\frac{L}{\delta} \right)^2 \right]} \tag{43}$$

with δ, skin depth: $\delta = \sqrt{2/(\sigma\mu\omega)}$ (44)

Because the characteristics of RFEC are explained through an analytical approach, and detection of a defect and quantitative analysis were done in Section 1.1, the effect of the moving conductor on the flux density is described directly by the results of finite-element analysis, omitting the closed-form solution.

Using the same excitation frequency and the same defect model as in previous analysis, the amplitude of the flux density according to each defect size (depth) is shown in Figure 6. The moving velocity of the exciter is 0.2 m/s, corresponding to a concept of inspection distance of 720 m per hour. This is feasible to inspect small-diameter and low-pressure pipelines. In this graph, we can see that the transition of the flux density increases as the depth of the defect increases from 12.5% to 87.5% in the same direction as the moving velocity and that the amplitude for detecting a defect decreases by about 10%, making the detection of a defect difficult when its depth is small. This graph is compared with the no-defect case as in Figure 4.

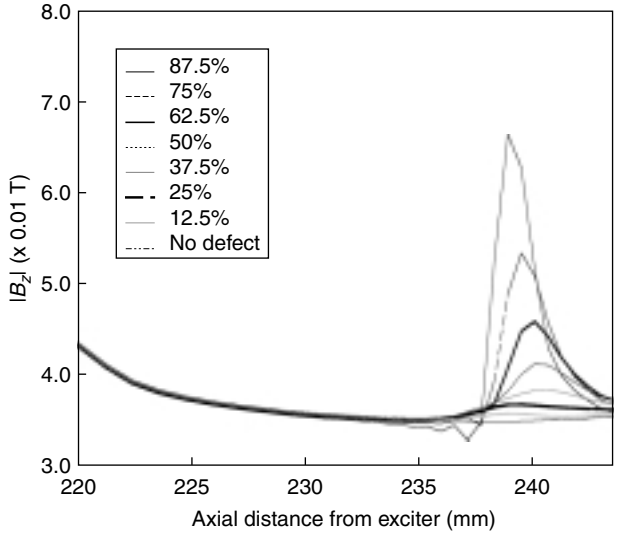

Figure 6

Amplitude of the flux density when the detector moves with 0.2 m/s (upper: defect of 87.5%; lower: defect of 12.5%).

Figure 7 is a result for a defect depth of 50% of the wall thickness of the pipe, which is relatively easy to detect. In this figure, we can see that detecting the attenuation of RFEC is possible at a velocity of 0.5 m/s, compared with depth of 12.5%, even though the shape of the flux density is transited in the moving direction. Therefore, from these results, it is important that, because the moving velocity causes a transition of the flux shape and a decrease in its amplitude, and furthermore weakens characteristics of RFEC, one must analyze the limit of the moving velocity and use the RFEC principle within this limit after defining the minimum detection size (depth) of a defect to wall thickness. This can be a kind of resolution concept.

Up to this point, all analyses are done with a constant excitation frequency. To maximize the magnetic vector potential and magnetic flux density for detection of a defect in the RFEC region, it is necessary to consider whether there is an optimal frequency for them because it means a maximization of the sensitivity of the detector for real implementation.

The excitation frequency ω in Equations (20) and (27) is related to the radial wave number k_{pr} and axial wave number k_{pz}. In other words, these are coupled with a concept of wave propagation by multiplication of conductivity, permeability, and frequency. Since it is not easy to obtain the optimum value of the excitation frequency analytically, even if there is, finite-element analysis is done for this.

As a result of varying excitation frequency, but using the same model and the same physical properties as in previous analysis, amplitude apparently seems to be increased as frequency is lowered and phase lag seems to be increased as frequency gets higher. But this value is not normalized with no-defect case to specific frequency. Then, Figure 8 represents the change of amplitude to no-defect case for each excitation frequency. The ratio of amplitude to no-defect case at a frequency of 1.7 Hz is larger than that at a frequency of 37 Hz. The result shows that there is no optimum frequency in real implementation range, but the sensitivity of the detection can be higher as the excitation frequency is lowered. As a matter of course, this lower frequency is also restricted by the inspection speed at real implementation.

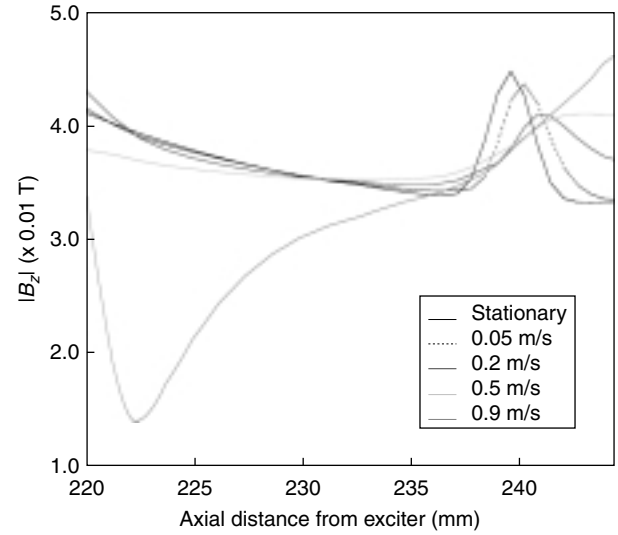

Figure 7

Velocity effect on the amplitude of the flux density (defect: 50% of the wall thickness; velocity: 0.05-0.9 m/s).

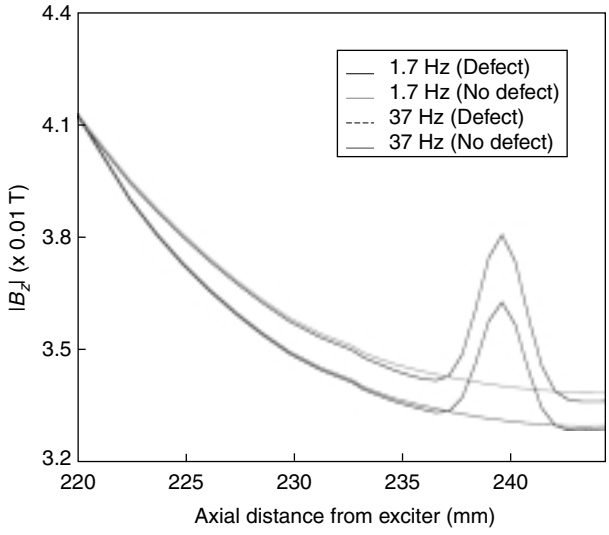

Figure 8

Comparison of the flux density change with varying excitation frequency (defect: 25% of the wall thickness; frequency: 1.7-37 Hz).

2 CHARACTERISTICS OF INDUCED VOLTAGE IN METAL DEFECTS

2.1 Analysis of Induced Voltage

Up to now, amplitude and phase changes of the magnetic flux density have been analyzed when there was a defect. But the magnetic flux density is not convenient to be measured, while the induced voltage is more suitable to be measured in a detector coil. The following description is based on the induced voltage through finite-element analysis and experimental work for real measurement.

We consider the flux passing through an arbitrary surface in a certain space where an arbitrary surface means a circular area in a real detector coil, as shown in Equation (45), which represents a relation between magnetic flux density and electric field intensity. This can be transformed after integration over surface area S (Popovic and Popovic, 1999):

$$\int_S (\nabla \times E) \cdot \mathrm{d}s = -\int_S \frac{\partial B}{\partial t} \cdot \mathrm{d}s \tag{45}$$

Applying Stoke's theorem, which converts surface integral into line integral, to Equation (45):

$$V = \oint_C E \cdot \mathrm{d}l = -\int_S \frac{\partial B}{\partial t} \cdot \mathrm{d}s \tag{46}$$

The left-hand term means induced voltage or EMF (electromotive force) in real measurement and it is derived from the change (amplitude or direction) of the flux density with time, passing through this surface area. This is called *Faraday's law* and in Equation (46), minus means opposite direction; in other words, electric field is induced to decrease its magnitude when the flux increases and to increase when the flux decreases. That is *Lenz' law*. It is important to measure the induced voltage generated by Equation (46) to detect and estimate quantitatively a defect in real implementation. A schematic diagram to measure the induced voltage is shown in Figure 9. A function generator for generating a sine wave is connected to a power amplifier to supply current into the exciter coil located coaxially with the pipe. A detector located $2D$ away from the exciter coil measures the induced voltage by interaction of the indirect field or RFEC. This signal is transmitted to a lock-in amplifier (Standford Research Systems, 1999) and compared with a reference signal from the function generator, obtaining a phase difference.

The induced voltage is also transmitted to an oscilloscope after amplification in a pre-amplifier, which has functions of high-pass and low-pass filtering.

Before deriving the induced voltage, it is necessary to formulate the magnetic flux density analytically. Consider an exciter coil composed of outer radius b, inner radius a, and thickness t. Then, to compute the axial magnetic flux

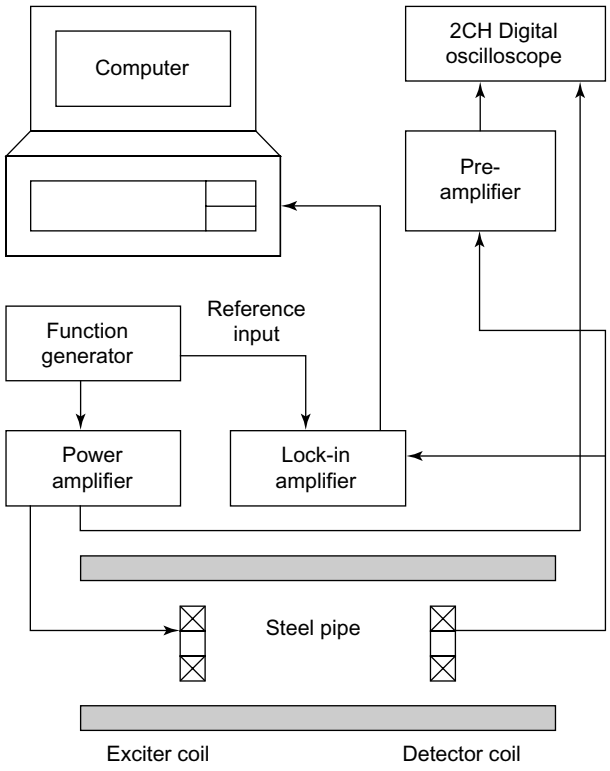

Figure 9

Schematic diagram of the RFEC measurement system.

density ($\boldsymbol{B}$) from Biot-Savarrt's law, the infinitesimal current density becomes $J\ \mathrm{d}z\ t\ (a + z)$ at angle φ and radius z. Therefore, the axial flux density $\boldsymbol{B}$ is represented as in Equation (47) and the cross-product of the two vectors is shown in Equation (48). tan θ and cos θ are simplified in Equations (49) and (50), and the distance X from the source current to the concerned region is presented in Equation (51):

$$\boldsymbol{B}(r) = \frac{\mu_0}{4\pi} \int_0^{2\pi} \int_0^{b-a} \frac{(J\mathrm{d}z\ t)\ (a + z)\ \mathrm{d}\varphi\ (\tilde{e}_\theta \times \tilde{e}_r)}{X^2} \tag{47}$$

$$\tilde{e}_\theta \times \tilde{e}_r = \cos(\theta - \varphi) \tag{48}$$

$$\tan\theta = \frac{(a + z)\ \sin\varphi}{(a + z)\cos\varphi - r} \tag{49}$$

$$\cos(\theta - \varphi) = \frac{\left((a + z)\cos\ \varphi - r\right)\ \cos\varphi + (a + z)\sin^2\varphi}{\sqrt{\left((a + z)\ \cos\varphi - r\right)^2 + (a + z)^2 \sin^2\varphi}} \tag{50}$$

$$X^2 = \left((a + z)\cos\varphi - r\right)^2 + (a + z)^2 \sin^2\varphi \tag{51}$$

From Equations (47)-(51), $\boldsymbol{B}(r)$ is represented by Equation (52) after analytical integration (Zwillinger, 1996) in the first integral.

$$\boldsymbol{B}(r) = \frac{\mu_0 I}{4\pi(b-a)} \int_0^{2\pi} \left\{ \frac{a}{\sqrt{a^2 + r^2 - 2ar\cos\varphi}} - \frac{b}{\sqrt{b^2 + r^2 - 2br\cos\varphi}} - \log\left[a - r\cos\varphi + \sqrt{a^2 + r^2 - 2ar\cos\varphi}\right] + \log\left[b - r\cos\varphi + \sqrt{b^2 + r^2 - 2br\cos\varphi}\right] \right\} d\varphi \quad (52)$$

Next, from the magnetic flux density, the induced voltage is derived by Equation (46). The relation between voltage and current in the coil when current is supplied or voltage is induced is as follows:

$$V = L \frac{dI}{dt} + R I \quad (53)$$

where V is the voltage in the coil, I is the current, R is the resistance, and L is the inductance. In the exciter coil, the relation between voltage and current is as follows:

$$V = I\sqrt{R^2 + (\omega L)^2} \quad (54)$$

The exciter coil generates its current from voltage. Then it is needed to know the following impedance Z:

$$Z = \sqrt{R^2 + (\omega L)^2} \quad (55)$$

For this, the inductance L should be measured or calculated from the following Equation (56) (McMaster *et al.*, 1986):

$$L = 0.4\mu N^2[\ln(8a/r) - 2] \quad (56)$$

where μ is the permeability of the coil, N is the number of turns, a is the mean radius of the circular coil, and r means wire radius. The measured and calculated values of the inductance and impedance of the exciter and detector coils are shown in Table 1 and show good agreement.

TABLE 1

Calculated and measured values of the inductance and impedance of the exciter and detector (frequency: 50 Hz)

		R (Ω)	L (mH)	Z (Ω)
Exciter coil	Measured	4.67	6.21	5.06
	Calculated	5.03	7.27	5.52
Detector coil	Measured	69.78	44.31	71.19
	Calculated	77.11	52.2	78.83

The phase change of the induced voltage or EMF should be compared with reference to the exciter voltage. When the exciter is excited by a constant current mode, this current shall be a form of $I = I_0 \exp(j\omega t)$ and the voltage V shall be a form of $V = I(R + jL\omega)$. Then, the phase of voltage V leads the current. However, in real implementation, the exciter coil is excited by a constant voltage mode when the function generator is used as shown in Figure 9, so that the phase of the current lags the voltage. Therefore, the current I is obtained by the impedance Z in Equation (55) from the reference voltage, and the phase difference between the exciter current and the exciter voltage is obtained by the following equation:

$$\Psi_E = -\tan^{-1}\left(\frac{\omega L}{R}\right) \quad (57)$$

By this exciter current, a flux density exists in accordance with permeability. In case of carbon steel (gas distribution pipeline), the relative permeability is very large compared with that of non-ferromagnetic materials such as stainless steel. Then the flux density is much larger than that of non-ferromagnetic materials. Because this ferromagnetic material also has electric conductivity, a series of phenomena, *e.g.* generation of flux density from permeability and induction of eddy current from conductivity, can occur.

Reviewing Equation (52), the phase of the flux density to the exciter current in air without pipe has ± 90° but cannot be estimated simply within the pipe because mixing of the direct and through-transmission fields makes it difficult to analyze. It is rather convenient to represent the flux density in a form of complex type:

$$B_z = B_0(r, \theta, z)\ e^{j\{\omega t + \Psi_B(r,\theta,z)\}} \quad (58)$$

$$B_z = Re\left[B_0(r, \theta, z)\ e^{j\{\omega t + \Psi_B(r,\theta,z)\}}\right] + j\,Im\left[B_0(r, \theta, z)\ e^{j\{\omega t + \Psi_B(r,\theta,z)\}}\right] \quad (59)$$

Equation (58) uses amplitude and phase forms in which Ψ_B is the phase to exciter current, and Equation (59) uses real and imaginary components, making easier to interpret results of finite-element analysis. Inserting Equations (58) and (59) into Equation (46) allows to derive the induced voltage *(V_D)* in the detector *(see below)*:

$$\frac{\partial B_z}{\partial t} = j\,\omega B_0(r, \theta, z)\ e^{j\{\omega t + \Psi_B(r,\theta,z)\}} = j\,\omega B_z = \omega\left(-Im\left[B_0(r, \theta, z)\ e^{j\{\omega t + \Psi_B(r,\theta,z)\}}\right] + jRe\left[B_0(r, \theta, z)\ e^{j\{\omega t + \Psi_B(r,\theta,z)\}}\right]\right)$$

$$V_D = \omega N\left(\int Im\left[B_0(r, \theta, z)\ e^{j\{\omega t + \Psi_B(r,\theta,z)\}}\right] dS - j\int Re\left[B_0(r, \theta, z)\ e^{j\{\omega t + \Psi_B(r,\theta,z)\}}\right] dS\right) \quad (60)$$

where the integration area S means the area of the detector coil. Apparently, the amplitude of induced voltage seems to be proportional to the exciter frequency, number of turns and flux density. The advantage of the excitation frequency on the induced voltage in Equation (60) is clear, but the flux density is also a function of this frequency in unknown manner, so that we cannot conclude simply. This is explained below. From Equation (60), the phase of the induced voltage $\Psi_{D\text{-}B}$ is:

$$\Psi_{D-B} = \tan^{-1}\left(\frac{-\int Re\left[B_0(r,\theta,z)\, e^{j\{\omega t+\Psi_B(r,\theta,z)\}}\right] dS}{\int Im\left[B_0(r,\theta,z)\, e^{j\{\omega t+\Psi_B(r,\theta,z)\}}\right] dS}\right) \quad (61)$$

Therefore, the phase $\Psi_{D\text{-}E}$ of induced V_D to the exciter reference V is as follows:

$$\Psi_{D-E} = \Psi_E + \Psi_{D-B} = -\tan^{-1}\left(\frac{\omega L}{R}\right) + \tan^{-1}\left(\frac{-\int Re\left[B_0(r,\theta,z)\ e^{j\{\omega t+\Psi_B(r,\theta,z)\}}\right] dS}{\int Im\left[B_0(r,\theta,z)\ e^{j\{\omega t+\Psi_B(r,\theta,z)\}}\right] dS}\right) \quad (62)$$

The specifications of the pipe material for computed induced voltage by finite-element analysis and for measuring by experiments are the following: operating pressure in gas distribution purpose is relatively low, with range of 200-5000 mm of H_2O, nominal diameter is 100 mm with outside diameter of 114 mm and inside diameter of 106 mm. The relative permeability is assumed to be 70 and the electric conductivity 7×10^6 (1/Ωm).

The *B-H* curve of this material is shown in Figure 10. In this figure, we can see that the range used in this RFEC is much less than the saturation point, so that there is no problem in analyzing the flux density within this range.

Some results are reviewed from three-dimensional finite-element analysis. Figure 11 shows the induced voltage obtained by finite-element analysis, in air without pipe for calibration purpose, and the induced voltage obtained by experimental measurement. About 2.8 V are applied to an exciter coil of 300 turns. The upper graph is obtained by integrating each complex component of the flux density with outer radius of the detector coil by applying Equation (60). Each value in this graph is 10% larger than that in the middle graph, which is obtained by using inside radius of the detector for integration path. This is due to the fact that the induced voltage increases according to the amplitude of the flux density and to the integration area passed through by the flux density as explained in Equation (46). Along the axial direction, the decrease rate is well suited to exponential form. The lower graph corresponds to the measured induced voltage and also shows the exponentially decreased form. From the fact that this measured value agrees well with finite-element results based on inside integration radius, within 20%, finite-element analysis is considered to be very reliable.

To describe induced voltage from flux density in detail, analytical formulations are presented again. Returning to the system model composed of the internal air-pipe-external earth and governing equations setup in Section 1.1, Hankel function shall be represented by a complex form:

$$H_n^{(1),(2)}(r) = \sqrt{\frac{2}{\pi(kr)}}\ e^{\pm j(kr-\pi/4-n\pi/2)} \quad (63)$$

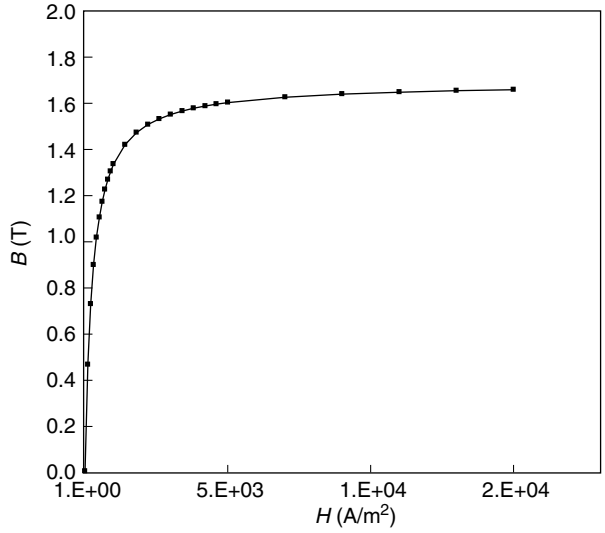

Figure 10

B-H curve of the carbon steel pipe.

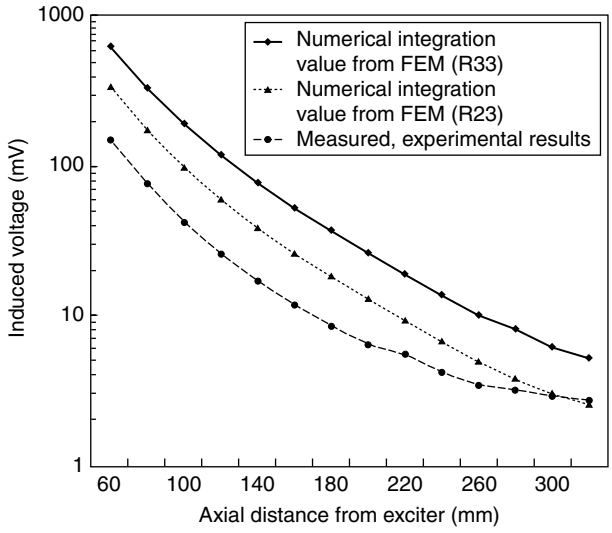

Figure 11

Plot of EMF in air from experimental and finite-element results.

Boundary conditions for far infinite region tell us that the Hankel function at this region should be zero. The axial wave number k is explained by $k = Re(k) + j\,Im(k)$ for convenience. Substituting this complex number into Equation (63) leads to:

$$H_n^{(1),(2)}(r) = \sqrt{\frac{2}{\pi(kr)}}\; e^{\pm j[\{Re(k)+j\,Im(k)\}r-\pi/4-n\pi/2]} \tag{64}$$

Restriction for the axial wave number k is:

$$Im(k) < 0 \tag{65}$$

After considering the compatibility condition on inner and outer pipe walls as shown in Equations (22)-(25), then the following linear equations should be satisfied:

$$[M]\,\{C\} = 0 \tag{66}$$

$$[M] = \begin{bmatrix} m_{11} & m_{12} & m_{13} & m_{14} \\ m_{21} & m_{22} & m_{23} & m_{24} \\ m_{31} & m_{32} & m_{33} & m_{34} \\ m_{41} & m_{42} & m_{43} & m_{44} \end{bmatrix} \tag{67}$$

$$\{C\}^T = \{c1\ c2\ c4\ c5\} \tag{68}$$

where $\{C\}$ is a coefficient vector for the magnetic vector potential related to the internal air-pipe-external earth and m_{ij} is each coefficient element for Bessel functions. Hence, the determinant of matrix $[M]$ should be zero in order to be satisfied for arbitrary coefficient c_{ij}:

$$\det [M] = 0 \tag{69}$$

On the other hand, each coefficient is obtained by Equation (66) through the normalizing as follows *(Eqs. (70)-(72))*:

$$\left(\frac{c2}{c1}\right) = \frac{k\,\mu_r\,J_0(kr_i)\,J_1(\alpha r_i) - \alpha\,J_0(\alpha r_i)\,J_1(kr_i)}{\alpha\,J_1(kr_i)\,Y_0(\alpha r_i) - k\,\mu_r\,J_0(kr_i)\,Y_1(\alpha r_i)} \tag{70}$$

$$\left(\frac{c5}{c1}\right) = \frac{J_0(\alpha r_i) + \left(\frac{c2}{c1}\right) Y_0(\alpha r_i)}{k\,\mu_r\,J_0(kr_i)} = \frac{J_1(\alpha r_i)\,Y_0(\alpha r_i) - J_0(\alpha r_i)\,Y_1(\alpha r_i)}{\alpha\,J_1(kr_i)\,Y_0(\alpha r_i) - k\,\mu_r\,J_0(kr_i)\,Y_1(\alpha r_i)} \tag{71}$$

Therefore, the magnetic flux densities for pipe, internal air and vector potential for external earth are given by Equations (73)-(75).

$$\left(\frac{c4}{c1}\right) = \frac{J_0(\alpha r_o) + \left(\frac{c2}{c1}\right) Y_0(\alpha r_o)}{k\,\mu_r\,\left(J_0(kr_o) - j\,Y_0(kr_o)\right)} = \frac{\left[-k\ \mu_r\,J_0(kr_i)\,J_1(\alpha r_i) + \alpha\,J_0(\alpha r_i)\,J_1(kr_i)\,Y_0(\alpha r_o)\right]}{\left[k\,\mu_r\,\left(J_0(kr_o) - j\,Y_0(kr_o)\right)\left(-\alpha\,J_1(kr_i)\,Y_0(\alpha r_i) + k\,\mu_r\,J_0(kr_i)\,Y_1(\alpha r_i)\right)\right]} \tag{72}$$

$$\frac{B_p(r)}{c1} = \frac{\left[\alpha\,J_1(kr_i)\left\{-J_0(\alpha r_i)\,Y_0(\alpha r) + J_0(\alpha r)\,Y_0(\alpha r_i)\right\} + k\,\mu_r\,J_0(kr_i)\left\{J_1(\alpha r_i)\,Y_0(\alpha r) - J_0(\alpha r)\,Y_1(\alpha r_i)\right\}\right]}{\left\{\alpha\,J_1(kr_i)\,Y_0(\alpha r_i) - k\,\mu_r J_0(kr_i)\,Y_1(\alpha r_i)\right\}} \tag{73}$$

$$\frac{B_i(r)}{c1} = \frac{k\,J_0(kr)\left\{-J_1(\alpha r_i)\,Y_0(\alpha r_i) + J_0(\alpha r_i)\,Y_1(\alpha r_i)\right\}}{-\alpha\,J_1(kr_i)\,Y_0(\alpha r_i) + k\,\mu_r\,J_0(kr_i)\,Y_1(\alpha r_i)} \tag{74}$$

$$\frac{A_e(r)}{c1} = \frac{H_1^{(2)}(kr)}{k\,\mu_r\left\{J_0(kr_o) - j\,Y_0(kr_o)\right\}}\left[J_0(\alpha r_o) + \frac{k\,\mu_r\,J_0(kr_i)\,J_1(\alpha r_i) + \alpha\,J_0(\alpha r_i)\,J_1(kr_i)\,Y_0(\alpha r_o)}{-\alpha\,J_1(kr_i)\,Y_0(\alpha r_i) + k\,\mu_r\,J_0(kr_i)\,Y_1(\alpha r_i)}\right] \tag{75}$$

Finally, the flux density for external earth is expressed in Equation (76). All quantities are normalized in Equations (73)-(76) by the unknown coefficient $c1$:

$$\frac{B_e(r)}{c1} = \frac{H_0^{(2)}(kr)}{\mu_r\left\{J_0(kr_o) - j\,Y_0(kr_o)\right\}}\left[J_0(\alpha r_o) + \frac{k\,\mu_r\,J_0(kr_i)\,J_1(\alpha r_i) + \alpha\,J_0(\alpha r_i)\,J_1(kr_i)\,Y_0(\alpha r_o)}{-\alpha\,J_1(kr_i)\,Y_0(\alpha r_i) + k\,\mu_r\,J_0(kr_i)\,Y_1(\alpha r_i)}\right] \tag{76}$$

To calculate the induced voltage from the magnetic flux density, it is necessary to decide the location and shape of the detector coil, since metal defects are divided into metal loss in the whole circumferential wall, and local pits in which a defect exists at a specific location (r, θ, z). In case of metal loss, the induced voltage is easy to be measured because the centerline axis of the pipe coincides with the axial detector. That is the reason why the integration path in Equation (46) is the same as the arbitrary circle through the centerline axis, and eventually each integration coordinate (r, θ) agrees with the coordinate of the flux density.

In case of local pits, it is not simple to derive the exact induced voltage. Let us assume that the detector coil of radius a is located ε away from the inner wall of the pipe of radius R, and that the flux density is distributed perpendicular to this plane, which is the axial direction. Then, the radial coordinate from pipe center to arbitrary location (r, θ) in the detector is:

$$\chi = \sqrt{(R - a - \varepsilon)^2 + r^2 + 2r\,(R - a - \varepsilon)\,\sin\theta} \tag{77}$$

The induced voltage is derived from Equations (46), (74) and (77) *(Eq. (78))*.

$$\text{EMF} = -\int_S j\,\omega\,B_i(r)\,\mathrm{d}S = -\int_0^{2\pi}\int_0^{a}\left\{\sqrt{(R-a-\varepsilon)^2 + r^2 + 2r\,(R-a-\varepsilon)\,\sin\theta}\; j\,\omega\,B_i\right\} r\mathrm{d}\theta\,\mathrm{d}r \tag{78}$$

To integrate the above function, it is helpful to approximate (Kreyszig, 1993) Bessel function in Equation (74) by:

$$J_n(x) = x^n \sum_{m=0}^{\infty} \frac{(-1)^m x^{2m}}{2^{2m+n}\,m!\;(n+m)!} \tag{79}$$

Therefore, in Equation (74), Bessel's function of argument which equals Equation (77) is approximated by Equation (80), and the induced voltage resulting from the time-variant flux density passing through the detector coil can be obtained from Equations (78), (80) and (74) *(Eqs. (80) and (81))*.

This induced voltage is really calculated if we know the axial wave number k. Hence, returning to Equation (69), a dispersion equation can be obtained from the coefficient matrix *(Eq. (82))*.

The solution to the dispersion Equation (82) is shown graphically in Figure 12. This figure shows one feasible solution for the complex axial wave number k with $Re(k)$ and $Im(k)$ matching the x-axis and y-axis, respectively, displaying minimum value (zero) of complex absolute magnitude to satisfy Equation (82) (Wolfram, 1997). In other aspect, Figure 13 shows the contour distribution for Figure 12, representing an optimal point for Equation (82). As a matter of course, due to the dispersion property of the axial wave number k (Silvester and Pelosi, 1994), there are infinite solutions beside the k in Figure 12.

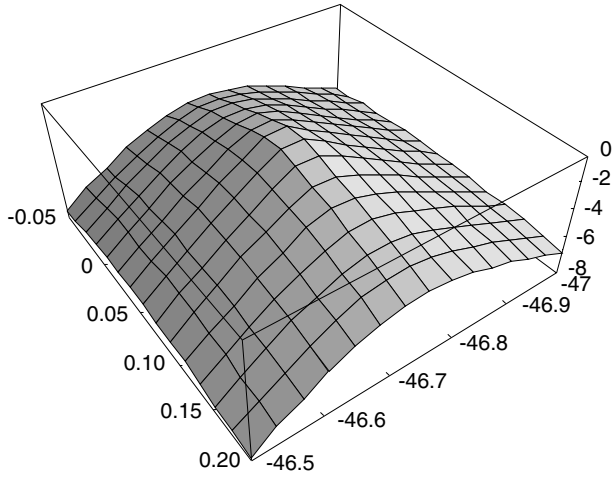

Figure 12

Complex absolute value of det [M] for finding $k = Re(k) + j\,Im(k)$.

$$J_0(k\chi) = \sum_{m=0}^{\infty}\left[\frac{\left\{(R-a-\varepsilon)^2 + r^2 + 2r\,(R-a-\varepsilon)\right\}^m}{2^{2m}(m!)^2}\;(-1)^{2m}\sin\theta^{2m}k^{2m}\right] \tag{80}$$

$$\frac{\text{EMF}}{c1} = \frac{j\omega k\left\{-J_1(\alpha r_i)\,Y_0(\alpha r_i) + J_0(\alpha r_i)\,Y_1(\alpha r_i)\right\}}{\left\{\alpha\,J_1(kr_i)\,Y_0(\alpha r_i) - k\,\mu_r\,J_0(kr_i)\,Y_1(\alpha r_i)\right\}} \int_0^{2\pi}\int_0^{a}\left\{\sum_{m=0}^{\infty}\frac{\left[(R-a-\varepsilon)^2 + r^2 + 2r\,(R-a-\varepsilon)\right]^m}{2^{2m}(m!)^2}\;(-1)^{2m}k^{2m}\sin\theta^{2m}\right\} r\,\mathrm{d}\theta\,\mathrm{d}r \tag{81}$$

$$\begin{aligned}\det[M] = {} & J_1(kr_i)\left[k\,\mu_r\{J_0(kr_o) - j\,Y_0(kr_o)\}\left\{-\frac{J_1(\alpha r_o)Y_0(\alpha r_i)}{\alpha} + \frac{J_0(\alpha r_i)Y_1(\alpha r_o)}{\alpha}\right\}\right.\\ & + \left\{-J_0(\alpha r_o)Y_0(\alpha r_i) + J_0(\alpha r_i)Y_0(\alpha r_o)\right\}\left\{-J_1(kr_o) + j\,Y_1(kr_o)\right\}\Big]\\ & + k\,\mu_r\,J_1(kr_i)\left[-k\,\mu_r\left\{J_0(kr_o) - j\,Y_0(kr_o)\right\}\left\{-\frac{J_1(\alpha r_o)Y_1(\alpha r_i)}{\alpha^2} + \frac{J_1(\alpha r_i)Y_1(\alpha r_o)}{\alpha^2}\right\}\right.\\ & + \left\{-\frac{J_1(\alpha r_i)Y_0(\alpha r_o)}{\alpha} + \frac{J_0(\alpha r_o)Y_1(\alpha r_i)}{\alpha}\right\}\left\{-J_1(kr_o) + j\,Y_1(kr_o)\right\}\Big] = 0\end{aligned} \tag{82}$$

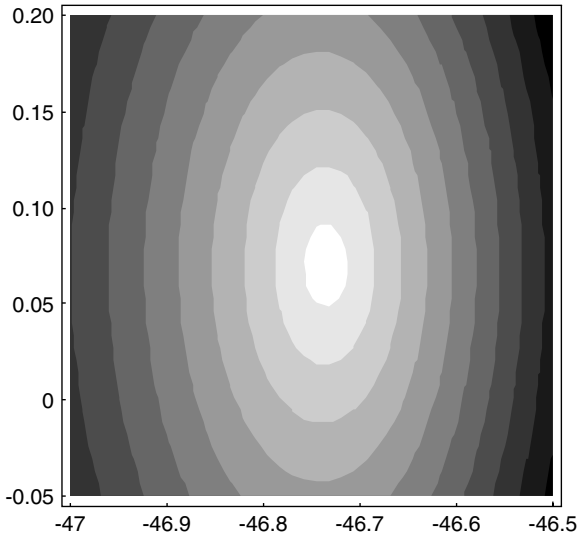

Figure 13

Solution point for the complex axial wave number *k*.

Figure 14 shows the magnetic flux density distribution in external earth from Equation (76) along the axial and radial directions, verifying convergency at an infinite boundary including axial and radial distances. The axial coordinate 0.2 m represents the remote field region that shall be used for interaction of flux density when there is a defect. Figure 15 shows the phase distribution of the flux density in external earth. The phase change along the radial direction is much larger than in the axial direction because the radial wave number α is much larger than the axial wave number k in Equation (83):

$$\alpha = \sqrt{k^2 - j\,\sigma\,\mu\,\omega} = \sqrt{k^2 - \frac{2j}{\delta^2}} \tag{83}$$

where δ is the skin depth (Silvester and Ferrari, 1983; Haugland, 1996), σ is the electric conductivity, and μ is the permeability. Because the excitation frequency is to make one radian phase lag at 50% of the wall thickness, the amplitude relation between the two wave numbers is:

$$\sqrt{Re(\alpha)^2 + Im(\alpha)^2} \gg \sqrt{Re(k)^2 + Im(k)^2}$$

2.2 Characteristics of Induced Voltage

Until now, the feasibility of the detection of metal defects is verified through the RFEC principle which causes amplitude and phase changes in induced voltage at a defect region, in which most metal defects, including cracks and pits, are dominant in the outer surface of the pipe, especially in case of city gas pipelines normally buried because of their electrochemical reaction between the pipe material and infinitesimal current flowed from external environment. The important thing is that change of the magnetic flux density is the key point to detect a metal defect in analysis, but in real implementation the voltage induced from the flux density should be measured, otherwise it is difficult to measure the flux density directly.

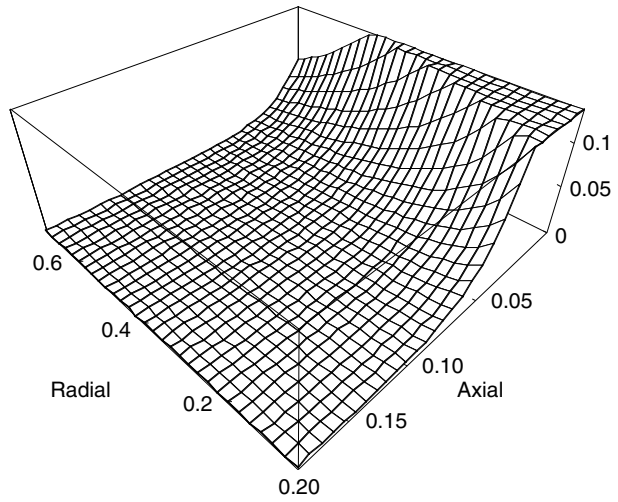

Figure 14

Amplitude distribution of | *Be*(*r*, *z*) |.

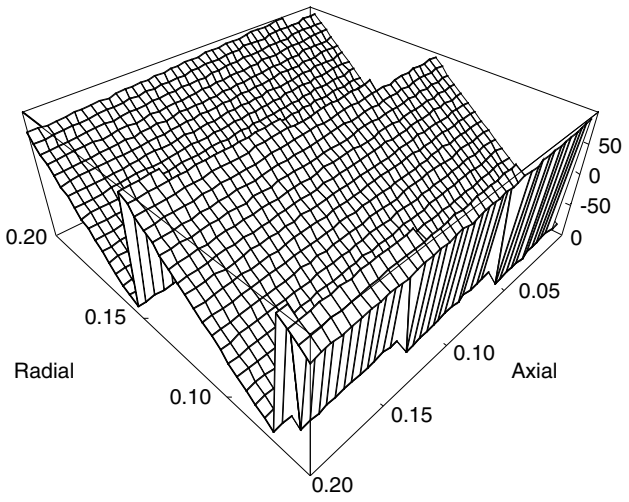

Figure 15

Phase distribution of *Be*(*r*, *z*).

The induced voltage in Equation (81) derived in Section 2.1 is reviewed again. Fundamental source to generate induced voltage in Equation (81) is based on Faraday's law with direction followed by Lenz' law. The induced voltage is the internal magnetic flux density $B_t(r)$ in Equation (74) transmitted through the flux density $B_p(r)$ in Equation (73) at the pipe wall from external field, in which the continuity of the magnetic field intensity is satisfied towards the tangential direction.

The physical parameters related to Equation (81) are permeability, electric conductivity, inside and outside diameters of the pipe material, current, impedance, number of turns, excitation frequency of the exciter coil, inductance and number of turns of the detector coil. In real measurement, it is helpful to maximize the induced voltage, but there are restrictions since most parameters are fixed and furthermore current or electric power is limited. As a matter of course, the ratio of signal to noise should be improved electronically. For convenience, it is possible to decrease the impedance of the exciter coil so that it results in a flowing current in given voltage (increased flux density generated in the system), and to maximize the number of turns and inductance of the detector coil.

If this type of work (*i.e.*, increase of the induced voltage) is performed, then the next step consists in using the RFEC principle to verify a relation between the defect size and the changes in the amplitude and phase of the induced voltage.

The meaning of a defect is local wall thinning. This results in changes of all parameters in Equation (81) in which there seems to be only a change of the outside radius, apparently. In the dispersion equation as in Equation (82), change of the outside radius r_o means a change of the axial wave number k for this equation to be satisfied in new circumstances. Next, the induced voltage changes as the internal flux density $B_t(r)$ changes in accordance with change of coefficient *c5* in Equation (71) resulting from a new radial wave number.

This phenomenon can be called a kind of interrelation. It is not simple to formulate it theoretically. In general, to represent this phenomenon, it is required to overcome three-dimensional dependence, non-linearity of material related to field, space and time, and finally discontinuity properties to complicated geometry (Palanisamy, 1987).

It is difficult to interpret Equation (81) when there is a defect compared with no defect, because it does not tell us how a change of amplitude and phase occurs in a simple manner. In case of the magnetic flux density, this study shows that the detection of metal defects is possible and a quantitative analysis is helpful to figure out a defect size from the fact of amplitude and phase change in the internal air adjacent to the inner wall of the pipe, when there is a defect. But in case of the induced voltage, this quantity is a result of integration of change rate of flux density (time derivative) with space coordinates such as area and location of the detector coil, *i.e.*, conversion of its phase by 90°. In other words, we can say that the induced voltage is converted from point vector of flux density to a scalar value whose characteristics are averaged by an area.

It is not possible to expect a relation between magnetic flux density having a coordinate value and induced voltage having no coordinate value without point integration area. Theoretically, a point detector is possible and the detection sensitivity can be maximized, but it is impossible to be realized. Therefore, in this study, the relation between the induced voltage and defects shall be presented through three-dimensional finite-element analysis and experimental work. Then, Equation (82) shall be analyzed by a simplification process.

Figure 16 shows the induced voltage measured by an axial detector coil (800 turns, inductance of 75 mH) located 2*D* away from the exciter coil (impedance of 6.6 Ω, 300 turns, inside diameter of 23 mm, outside diameter of 33 mm, and width of 10 mm) located coaxially with the pipe (outside diameter of 114 mm, inside diameter of 106 mm). To this exciter coil, a sine wave of 2 Vrms is applied *via* the function generator. The horizontal axis concerns the reference voltage, which is the excitation voltage in the exciter, and the vertical axis represents the induced voltage in the detector coil. In this figure, an ellipse is generated in real time due to the phase difference between the induced voltage and the reference voltage. As a matter of fact, the perfect shape of the ellipse is only theoretical and in real measurement, there are other factors to affect its shape, like noise, etc. The induced voltage measured within the pipe is relatively lower than that measured without pipe, because the flux density decreases within the pipe due to the energy transfer to relatively high-permeable pipe material (relative permeability of 70). In other words, the resistance is high in air only. When there is a defect, to detect and analyze it quantitatively, confirmation of the amplitude increase and of the phase lag is necessary as explained previously. For this, it is required to examine whether the size of the ellipse is changed. In case of in-phase state, the ellipse shrinks to a form of line.

Next, results of three-dimensional finite-element analysis are presented in the sequence of single-axial detector, metal loss (whole circumferential wall loss), and multi-axial

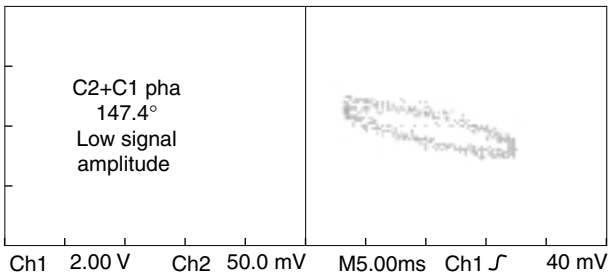

Figure 16

Measurement of the induced voltage (EMF) in the detector.

detector. An artificial defect (a kind of pit) is simulated by dimensioning 5.6, 1.6, and 2.4 mm in length (axial direction), width (circumferential direction), and depth (radial direction). A current of 4 A is applied to an exciter coil composed of inside diameter of 23 mm, outside diameter of 33 mm, width of 10 mm, number of turns of 300, and impedance of 6.6 Ω. The detector coil is composed of inductance of 50 mH, number of turns of 800, and diameter of 65 mm and is located axially within the pipe. The result shows that there is no detectable change of the induced voltage, which is derived in Equations (60), (62) and (81). This result is interpreted as follows: from the viewpoint of flux density, there is a definite difference in a defect model, but the induced voltage is averaged because the detector coil in this case is located coaxially within the pipe, and from Equation (60) there are some changes in the integrated value. This means that regarding integration path in Equation (60), the area for non-changed flux density is much larger than that for changed flux density, since a selective integration area is impossible in this type of single-axial detector coil. This effect is severe since the defect is as small as a pit (very small hole).

To confirm these characteristics of single-axial detectors for such a small defect, finite-element analysis is done again for metal loss. Metal loss means whole circumferential wall thinning and it is expected to be detected with the same single-axial detector as previously.

The dimensions of wall loss are identical to the previous model, except length (circumferential direction): a width of 1.6 mm and a depth of 2.4 mm (25% of pipe wall thickness) are used. Consequently, the flux density (axial direction) is more concentrated than in the case of pit due to the expanded area by whole circumferential direction at the inner wall of the pipe. The result shows about 20% of flux density increase. Then, the induced voltage from this increase of flux density is as follows: induced voltage is computed by Equation (60) from finite-element result. A change of the amplitude in the induced voltage is 1.5% and a change of the phase in the induced voltage by Equation (62) is 9.3%. This value is relatively larger than in case of a pit, but in respect to an integration path, the annular area is used instead of a central area, excluding an unaffected area (non-changed area for flux density). Therefore, it shows that a single-axial detector can detect a defect like a metal loss rather than a local pit. However, it is still not sufficient to detect a pit.

For purpose of detecting a pit, this study suggests a multi-axial detector coil. This pit should be detected in gas distribution pipelines because it is very dangerous to pipelines with possibility of growing larger hole or crack, even though there is no leak. In other aspect, this should be discovered for replacement or maintenance. For this purpose, a finite-element model is developed as shown in Figure 17. In this figure, a pit is simulated by length of 5.6 mm in circumferential direction, width of 1.6 mm in axial, and depth of 2.4 mm in radial direction (60% of the wall thickness).

The dimensions of the exciter coil are as follows: inside and outside diameters are 23 and 33 mm, width is 10 mm. Total 2.8 A with excitation frequency of 120 Hz are applied to the exciter coil with 300 turns from the power amplifier. This frequency means a skin depth of half wall thickness (2 mm). The current density is calculated from this source current divided by a cross-sectional area of the exciter coil, and its directions in circumference and magnitude are shown graphically in Figure 18.

The repeated circular area at internal air below the pipe wall in Figure 17 represents the multi-axial detector coil and this means integration area for the induced voltage in Equations (60) and (81).

As a result of finite-element analysis, Figure 19 shows the contour of a real (in-phase state with exciter's source current) component of the flux density and Figure 20 displays plot of

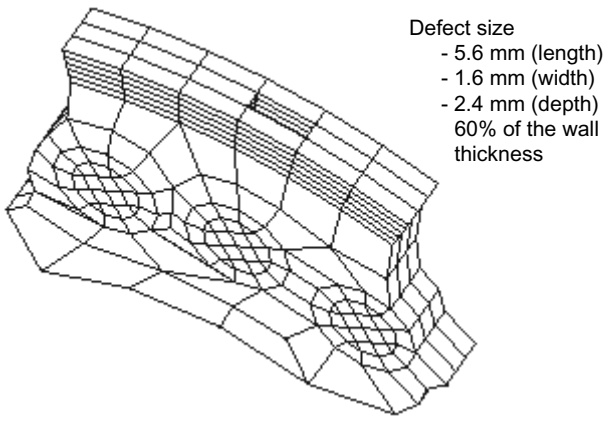

Figure 17

Local pit (defect) and integration area for the induced voltage.

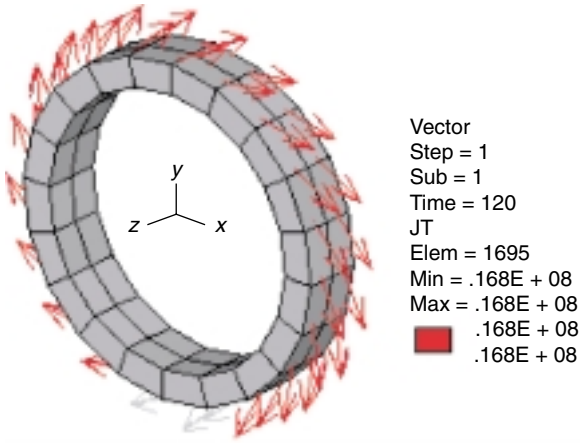

Figure 18

Finite-element model of the source current.

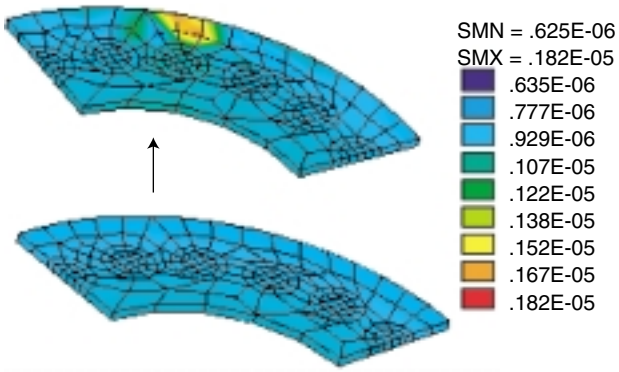

Figure 19

Plot of the real component of the flux density (upper: defect depth of 60%; lower: no defect).

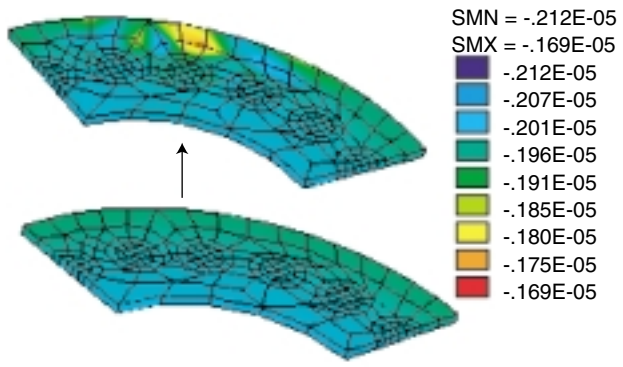

Figure 20

Plot of the imaginary component of the flux density: the phase change of the induced voltage is 9.3% (upper: defect depth of 60%; lower: no defect).

an imaginary component of the flux density. Each upper figure represents the contour when there is a defect and shows concentrated flux density due to a defect below the inner pipe wall. An effect of this increased density is also shown in the circular area, which is simulated for a multi-detector coil.

The resulting induced voltage through flux density in Figures 19 and 20 is obtained by Equations (60), (62) and (81). The phase difference between the defect model and the no-defect model is 9.3%, which is considerable. It clearly verifies that the detection of a pit and quantitative estimations are possible by using a multi-axial detector coil. This result leads to a point detector, which is ideal for a very tiny pit.

To validate these finite-element results, experimental works are done regarding measurement of the induced voltage. The exciter coil is the same as in the finite-element model, but the detector coil differs from the previous one. The inductance of this small multi-detector is 70 mH and the number of turns is 1700. This small coil is made of wire of 0.05 mm in diameter and internal ferrite core of which relative permeability is 2000. This detector is located 160 mm away from the exciter coil in the axial direction. In respect to the radial distance, this detector is positioned 10 mm away from the inner wall of the pipe for measurement, and 8 mm for finite-element analysis. As a result, at axial distance of 160 mm, the induced voltage by measurement is 0.36 mV which is a little lower than the finite-element result (0.76 mV) obtained by Equation (60). Regarding the phase difference, phase reading by measurement is 32.8° and that by finite-element analysis is 12.5°, which is obtained by Equation (62). We can see that the experimental measurements agree well to the finite-element results. In other words, finite-element analysis is very reliable compared to real measurements.

Figure 21 shows the induced voltage measured along the axial distance from the exciter coil with constant radial distance from the inner wall of the pipe (Atherton, 1995). This graph also shows similar trends with finite-element results. But there is considerable noise as the detector coil moves outward from the exciter coil, beyond 200 mm. In this noise environment, accurate measurements are not secured with non-repeatability and further experiments are discarded.

Finally, the effect of the excitation frequency on the induced voltage is not significant in the finite-element results. The excitation frequency directly affects the skin depth as shown in form of radial wave number in Equation (83). Therefore, if the frequency decreases, then the skin depth increases as an inverse ratio of square root and more flux is generated at the outer wall of the pipe, but this does not

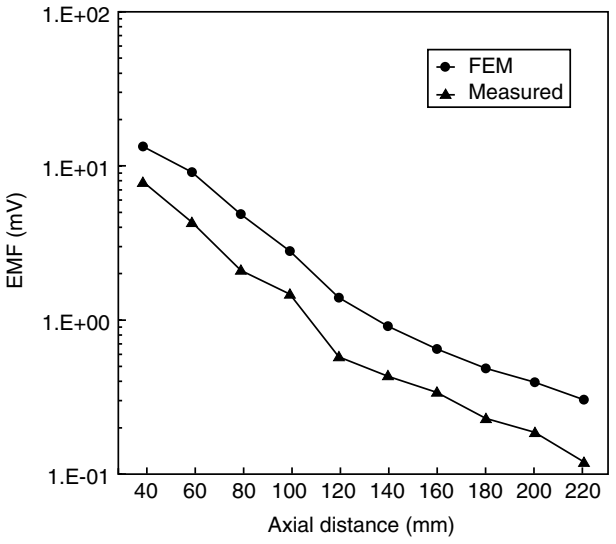

Figure 21

Amplitude of EMF along the axial distance.

contribute to increase the induced voltage. Until now, commercial software Ansys (Ansys User's Manual, 1995) was used for finite-element analysis.

CONCLUSION

In order to formulate Maxwell's equations, which are bases for detection of metal defects, the generalization of a magnetic vector potential and magnetic flux density is introduced, including both axial and radial wave numbers. An analytical approach shows that the detection of metal defects is possible by verifying the change of the amplitude and phase when there is a defect with the RFEC principle. The analytical approach has an advantage of understanding the role of key parameters on changes in the magnetic flux density, consequent induced voltage, and dispersion relation shown in Equations (27), (81) and (82), respectively, when there is a defect. Physical interactions between the defect case and the no-defect case can be explained intuitively from this analytical solution. However, in case of a small pit and furthermore complicated geometry, obtaining an exact solution is very difficult and tedious. This is the reason why finite-element analysis is used, in which the distribution of the magnetic vector potential and magnetic flux density are obtained by Maxwell's equation, and changes in the amplitude and phase of the induced voltage can be obtained by Equations (60) and (62).

Three-dimensional finite-element analysis is presented to overcome an inappropriateness of the axisymmetry condition often used in two-dimensional analysis. It shows that a very small pit can be simulated with consideration of circumferential dependence and wave propagation in this direction, otherwise only whole metal loss can be detected. Another benefit is that it can eliminate inaccuracy occurring in using Neumann, Dirichlet, and cyclic symmetry conditions for boundary.

For real implementation as in in-pipe robot, the effect of the detector velocity on the amplitude of the magnetic flux density is presented. For this purpose, the velocity-induced current in such a conductive material as a pipe is introduced and stationary coordinate is used not to exclude time variant of magnetic flux. The result suggests a criterion to the limiting velocity for an arbitrary defect to be detected, verifying the transition and distortion of the amplitude of the flux density.

Finally, for measurement and analysis, characteristics of the induced voltage are explained analytically and a computation method of the induced voltage from finite-element analysis is presented, hence showing good results compared with experimental measurement. A multi-axial detector coil is suggested to detect a very small, local pit, verifying significant changes in amplitude and phase. Eventually, it shall be a form of a point detector.

REFERENCES

Allen, N., Rodger, D. and Coles, P.C. (1995) Towards Increased Speed Computations in 3D Moving Eddy Current Finite Element Modeling. *IEEE Transactions on Magnetics*, **31**, 6, 3524-3526.

Ansys User's Manual (1995) *Electromagnetics*, Revision 5.2, SAS IP.

Atherton, D.L. (1995) Remote Field Eddy Current Inspection. *IEEE Transactions on Magnetics*, **31**, 6, 4142-4147.

Atherton, D.L. and Czura, W. (1994) Finite Element Calculations for Eddy Current Interactions with Collinear Slots. *Materials Evaluation*, January, 96-100.

Atherton, D.L. *et al.* (1987) The Applications of Finite Element Calculations to the Remote Field Inspection Technique. *Materials Evaluation*, **45**, 9, 1083-1086.

Atherton, D.L., Sullivan, S. and Daly, M. (1988) A Remote-Field Eddy Current Tool for Inspecting Nuclear Reactor Pressure Tubes. *British Journal of Non-Destructive Testing*, **30**, 1, 22-28.

Atherton, D.L., Czura, W.L. and Mackintosh, D.D. (1994) Remote Field Eddy Current Defect Interactions: Effects on the External Field. *Materials Evaluation*, November, 1288-1291.

Brown, R.H. and Jaroudi, M. (1992) Torque Prediction and Maximization Strategies for Bifilar-Wound Hybrid Step Motors. *IEEE Transactions on Power Electronics*, **7**, 3, 535-541.

Chen, M., Sun, Y., Lord, W. and Shin, Y.K. (1992) Pulsed RFEC Probe Response. *IEEE Transactions on Magnetics*, **28**, 2, 1430-1433.

Gustafson, K.E. (1980) *Introduction to Partial Differential Equations and Hilbert Space Methods*, John Wiley & Sons.

Haugland, S.M. (1996) Fundamental Analysis of the Remote-Field-Eddy-Current Effect. *IEEE Transactions on Magnetics*, **32**, 4, 3195-3211.

Hildebrand, F.B. (1976) *Advanced Calculus for Applications* (2nd ed.), Prentice Hall.

Ida, N. and Bastos, J.P.A. (1997) *Electromagnetics and Calculation of Fields* (2nd ed.), Springer Verlag.

Kawaguchi, Y., Yoshida, I., Kurumatani, H., Kikuta, T. and Yamada, Y. (1995) Internal Pipe Inspection Robot. *IEEE International Conference on Robotics and Automation*, 857-862.

Kreyszig, E. (1993) *Advanced Engineering Mathematics* (7th ed.), John Wiley & Sons.

Liu, Z., Dawson, G.E. and Eastham, T.R. (1995) Modeling Moving Conductor Eddy Current Problems with Edge Elements. *IEEE Transactions on Magnetics*, **31**, 6, 3521-3523.

Lord, W., Sun, Y.S. *et al.* (1988) Physics of Remote Field Eddy Current Effect. *Review of Progress in Quantitative Non-Destructive Evaluations*, Thomson, D.O. and Chimenti, D.E. (eds.), **7A**, Plenum Press, New York.

Lowther, D.A. and Silvester, P.P. (1985) *Computer-Aided Design in Magnetics*, Springer Verlag.

Mackintosh, D.D., Atherton, D.L. and Puhach, P.A. (1993) Through-Transmission Equations for Remote-Field Eddy Current Inspection of Small-Bore Ferromagnetic Tubes. *Materials Evaluation*, June, 744-748.

Mandayam, S., Udpa, L., Udpa, S.S. and Lord, W. (1996) Invariance Transformations for Magnetic Flux Leakage Signals. *IEEE Transactions on Magnetics*, **32**, 3, 1577-1580.

McMaster, R.C., McIntire, P. and Mester, M.L. (1986) *Nondestructive Testing Handbook* (2nd ed.), **4**, Electromagnetic Testing, American Society for Nondestructive Testing.

Mergelas, B.J. and Atherton, D.L. (1996) Discontinuity Interaction and Anomalous Source Models in Through

Transmission Eddy Current Testing. *Materials Evaluation*, January, 87-92.

Muramatsu, K., Nakata, T. and Fujiwara, K. (1992) Comparison of Coordinate for Eddy Current Analysis in Moving Conductors. *IEEE Transactions on Magnetics*, **28**, 2, 1186-1189.

Palanisamy, R. (1987) Theoretical Prediction of Remote-Field-Eddy-Current Response for the Nondestructive Evaluation of Metallic Tubes. *Journal of Applied Physics*, **61**, 8, 3202-3204.

Popovic, Z. and Popovic, B.D. (1999) *Introductory Electromagnetics* (1st ed.), Prentice Hall.

Schmidt, T.R. (1984) Remote Field Eddy Current Inspection Technique. *Materials Evaluation*, **42**, 2, 225-230.

Silvester, P.P. and Ferrari, R.L. (1983) *Finite Elements for Electrical Engineers* (1st ed.), Cambridge University Press.

Silvester, P.P. and Pelosi, G. (1994) *Finite Elements for Wave Electromagnetics: Methods and Techniques. A Selected Reprint Volume*, IEEE Antennas and Propagation Society, Sponsor, IEEE Press.

Song, H. and Ida, N. (1992) Modeling of Velocity Terms in 3D Eddy Current Problems. *IEEE Transactions on Magnetics*, **28**, 2, 1178-1181.

Standford Research Systems (1999) *Model SR830 DSP Lock-In Amplifier*, Revision 1.5, Standford Research Systems.

Sun, Y.S. (1989) A Finite Element Study of Diffusion Energy Flow in Low Frequency Eddy Current Phenomena. *Materials Evaluation*, **47**, 1, 87-92.

Sun, Y.S., Lin, H.Y., Chen, M.J. and Wang, C.D. (1992) Finite Element Modeling and Physics of Remote Field Eddy Current: Responses for Axially Aligned Cracks. *IEEE Transactions on Magnetics*, **28**, 4, 1941-1947.

Sutherlande, J. and Atherton, D.L. (1997) Effects of Bending Stresses and Tube Curvature on Remote Field Eddy Current Signals. *Materials Evaluation*, January, 85-89.

Theodoulidis, T.P. and Tsiboukis, T.D. (1995) Analytical Solutions in Eddy Current Testing of Layered Metals with Continuous Conductivity Profiles. *IEEE Transactions on Magnetics*, **31**, 2254-2260.

Wolfram, S. (1997) *Mathematica: A System for Doing Mathematics by Computer* (3rd ed.), Addison Wesley.

Woodson, H.H. (1968) *Electromechanical Dynamics*, *Part II: Fields, Forces, and Motion*, John Wiley & Sons.

Zwillinger, D. (1996) *Standard Mathematical Tables and Formulae* (30th ed.), CRC Press.

Final manuscript received in March 2001